

The relation between specific baryon angular momentum and mass for a sample of nearby low-mass galaxies with resolved H I kinematics

E. C. Elson,¹★

¹*Department of Astronomy, University of Cape Town, Private Bag X3, Rondebosch 7701, South Africa.*

15 October 2018

ABSTRACT

This paper investigates the relationship between specific baryon angular momentum j_b and baryon mass M_b for a sample of nearby late-type galaxies with resolved H I kinematics. This work roughly doubles the number of galaxies with $M_b \lesssim 10^{10} M_\odot$ used to study the $j_b - M_b$ relation. Most of the galaxies in the sample have their baryon mass dominated by their gas content, thereby offering j_b and M_b measures that are relatively unaffected by uncertainties arising from the stellar mass-to-light ratio. Measured H I surface density radial profiles together with optical and rotation curve data from the literature are used to derive a best-fit relation given by $j_b = qM_b^\alpha$, with $\alpha = 0.62 \pm 0.02$ and $\log_{10} q = -3.35 \pm 0.25$. This result is consistent with the $j_b \propto M_b^{2/3}$ relation that is theoretically expected and also measured by [Obreschkow & Glazebrook \(2014\)](#) for their full sample of THINGS spiral galaxies, yet differs to their steeper relation found for subsets with fixed bulge fraction. The 30 arcsec spatial resolution of the H I imaging used in this study is significantly lower than that of the THINGS imaging used by [Obreschkow & Glazebrook \(2014\)](#), yet the results presented in this work are clearly shown to contain no significant systematic errors due to the low-resolution imaging.

Key words: galaxies: fundamental parameters – galaxies: evolution

1 INTRODUCTION

Important insights into the structural properties, formation histories and dark matter halo properties of galaxies can be gleaned from their angular momentum properties. In the hierarchical galaxy formation scenario, angular momentum is thought to be transferred to collapsing proto-galaxies by the tidal field associated with an irregular matter distribution ([Peebles 1969](#)).

For stellar disks, [Takase \(1967\)](#) and [Freeman \(1970\)](#) were the first to study the link between total angular momentum J_* and mass M_* , finding a power law relation $J_* \propto M_*^{7/4}$. [Fall \(1983\)](#) was the first to study the distribution of galaxies in the $j_* - M_*$ plane, where $j_* \equiv J_*/M_*$ is the stellar specific angular momentum. He showed a sample of spirals to follow the power-law relation $j_* \propto M_*^\alpha$, with $\alpha \approx 0.6$. He also showed a sample of ellipticals to follow a roughly parallel trend in the $\log_{10} j_* - \log_{10} M_*$ plane, yet one which is roughly a factor of 6 lower. [Romanowsky & Fall \(2012\)](#) furthered the work of [Fall \(1983\)](#) by estimating j_* from kinematic and photometric data that extended to large radii and

M_* from near-infrared luminosities. They found the ellipticals and spirals to form two parallel $j_* - M_*$ tracks, with log-slopes of ~ 0.6 . [Fall & Romanowsky \(2013\)](#) re-visited the work of [Romanowsky & Fall \(2012\)](#) by considering the effects of variable near-infrared stellar mass-to-light ratios correlated with $B - V$ colours. They found both disk-dominated and elliptical galaxies to have $\alpha = 0.6 \pm 0.1$, but the offset between sequences increased by about 30 per cent.

The studies of [Fall \(1983\)](#); [Romanowsky & Fall \(2012\)](#); [Fall & Romanowsky \(2013\)](#) estimated j_* from velocity width measurements together with an assumption about the shape of the rotation curve. [Obreschkow & Glazebrook \(2014\)](#) were the first to measure J by integrating dJ over spatially and kinematically resolved observations of galaxies. Furthermore, [Obreschkow & Glazebrook \(2014\)](#) were the first to consider the contribution of gas (atomic and molecular) to J , in addition to the stellar contribution. For a sample of 16 spiral galaxies from THINGS, they demonstrated a strong correlation between baryon mass M_b , specific baryon angular momentum j_b , and bulge mass fraction β . In the $j_b - M_b$ plane, their data are consistent with the range of theoretically predicted (j_b, M_b) values for “isolated spiral galaxies evolved without major mergers, abnormal feedback, or oth-

★ E-mail: elson.e.c@gmail.com

erwise exotic histories”. Their power-law relation $j_b \propto M_b^\alpha$, with $\alpha \approx 2/3$, therefore also reproduces the exponent found by Romanowsky & Fall (2012) who considered only the stellar components of j_b and M_b . However, for a fixed bulge fraction, Obreschkow & Glazebrook (2014) find the residual scaling to have a power-law index $\alpha \approx 1$. This, they say, “implies that more massive spiral galaxies tend to have higher bulge fractions than less massive ones”.

All of the above-mentioned studies focussed on relatively high-mass galaxies. Until very recently, the $j - M$ relation for dwarf galaxies has remained unexplored. Butler et al. (2017) present measurements of j_b and M_b for a sample of 14 rotating dwarf Irregular galaxies from the LITTLE THINGS survey (Hunter et al. 2012). In gas-dominated systems with $M_b \lesssim 10^{10} M_\odot$, H I kinematics are required to measure the amount of angular momentum contained in the outer galaxy. Butler et al. (2017) find their dwarf galaxies to have systematically higher j_b values than expected from the $j_b \propto M_b^{2/3}$ scaling relation for spirals. They attribute this to a significantly steeper $j - M$ relation for H I, due to the systematic variation of H I fraction with M_b . Most recently, Chowdhury & Chengalur (2017) measured j_b and M_b for five gas-rich dwarf galaxies. They compare the $j_b - M_b$ distribution of their galaxies to the $j_b - M_b$ relation for the low-bulge-fraction ($\beta < 0.05$) subset of Obreschkow & Glazebrook (2014), and find the dwarfs to have significantly higher j_b . This, they say, suggests a difference in the evolution of angular momentum in the smaller galaxies, compared to the more massive spirals.

This work aims to further study the relation between j_b and M_b in a sample of 37 late-type and dwarf galaxies from the WHISP survey with spatially and kinematically resolved H I kinematics, thereby doubling the number of galaxies with $M_b \lesssim 10^{10} M_\odot$ studied in this context. Section 2 presents the data sets used to calculate j_b and M_b , while Section 3 details the specific methods of measuring the quantities. The results are presented together with a discussion in Section 4. Section 5 presents the details of a test carried out using THINGS imaging to quantify the significance of systematic errors in the j_b and M_b measures presented in this work. The conclusions of this study are given in Section 6.

2 DATA

The primary data set for this study comes from Swaters et al. (2009) who present rotation curves derived from H I observations for a sample of 62 dwarf galaxies observed as part of the Westerbork H I survey of Spiral and Irregular Galaxies (WHISP) project. From the full WHISP sample, Swaters et al. (2009) define as dwarfs all galaxies with Hubble type later than Sd, as well as spiral galaxies of earlier Hubble type with an absolute B -band magnitude fainter than -17 . The typical spatial resolution of their H I observations is $12'' \times 12''/\sin \delta$, where δ is the declination of the target. However, because the signal-to-noise ratios for most of their galaxies are too low to derive reliable rotation curves using standard methods, Swaters et al. (2009) use 30 arcsec resolution versions of their data to produce rotation curves. The reader is referred to Swaters et al. (2002) for the full details of the procedure used to produce the H I data cubes.

Swaters et al. (2009) adopt a two-step procedure to generate an initial estimate of each galaxy rotation curve. First, they attempt fitting a tilted ring model (Rogstad et al. 1974) to the velocity field of the galaxy. When this is not feasible, they use an interactive procedure to iteratively fit the rotation curve and orientation parameters to a set of six position-velocity diagrams from the observed data cubes. They then use this information to produce a three-dimensional model data cube which they compare directly to the data. The input rotation curve is interactively adjusted until a satisfactory comparison to the data is obtained. Swaters et al. (2009) determine the correction for asymmetric drift to be smaller than 3 km s^{-1} at all radii for all but three galaxies in their sample. Because the corrections are so small, they do not correct their measured rotation curves for asymmetric drift. The reader is referred to Swaters et al. (2009) for the full details of their procedure used to generate the rotation curves. Swaters et al. (2009) divide their derived rotation curves into four different categories of quality q . A reliable rotation curve is indicated by $q = 1$, whereas $q = 2$ and $q = 3$ indicate uncertain and highly uncertain rotation curves, respectively. Finally, $q = 4$ indicates a case for which no rotation curve could be derived.

Table 2 from Swaters et al. (2009) contains almost all of the data used in this work to calculate j_b and M_b for WHISP galaxies. It presents their rotation velocities at one, two, three, and four disk scale lengths, as well as the rotation velocity at the last measured point and the radius of the last measured point, R_{last} . It also lists the R -band properties from Swaters & Balcells (2002): absolute magnitude (corrected for Galactic foreground extinction, but not internal extinction), disk scale length, and central surface brightness. It presents the adopted distance for each galaxy (also discussed in Swaters & Balcells 2002). Not provided in Swaters et al. (2009) are the B -band absolute magnitudes of the galaxies. For this work, the B -band apparent magnitudes (corrected for extinction) are obtained from the Third Reference Catalog of Bright Galaxies, (RC3, de Vaucouleurs et al. 1991) and converted to absolute magnitudes using the distances listed in Swaters et al. (2009). The total H I masses and H I radii used in this work are taken from Table A.2 of Swaters et al. (2002). The 30 arcsec H I total intensity maps of the galaxies, available for download from <http://wow.astron.nl>, are used to derive an H I mass surface density profile for each galaxy (see Section 3.2).

The final sample of 37 WHISP galaxies used in this work consists of those galaxies in Swaters et al. (2009) with $q \leq 2$, inclination $i \leq 75^\circ$, a valid B -band apparent magnitude in RC3, and for which an H I total intensity map could be downloaded.

3 ANALYSIS

The optical and rotation curve data presented in Tables 2 and 3 of Swaters et al. (2009) together with the H I radius measurements from Swaters et al. (2002), the H I surface density profiles measured (in this work) from the 30 arcsec H I total intensity maps, and the B -band magnitudes from RC3 constitute all the information required to generate measures of the specific baryon angular momentum j_b and total baryon mass M_b for the galaxies. For each galaxy, M_b is cal-

culated by numerically evaluating the following integral:

$$M_b = \int_0^{R_{\text{HI}}} \Sigma_b(R) \cdot 2\pi R \cdot dR, \quad (1)$$

where R is galactocentric radius, R_{HI} is the radius at which the inclination-corrected H I mass surface density reaches $1 M_\odot \text{ pc}^{-2}$, and $\Sigma_b(R)$ is the baryon mass surface density in units of $M_\odot \text{ pc}^{-2}$. In this work, only the stellar, H I, and He contributions to the baryon mass are considered. The total baryon angular momentum J_b perpendicular to the disk of each galaxy is calculated as:

$$J_b = \int_0^{R_{\text{HI}}} 2\pi R \cdot \Sigma_b(R) \cdot V_{\text{PE}}(R) \cdot R \cdot dR, \quad (2)$$

where $V_{\text{PE}}(R)$ is a parameterisation of the observed H I rotation curve. The specific baryon angular momentum is then calculated as $j_b = J_b/M_b$.

The rest of this section presents the details of the procedures used to calculate $\Sigma_b(R)$ and $V_{\text{PE}}(R)$ for each galaxy.

3.1 Rotation curves

The circular velocity profile of each galaxy is obtained by fitting the measured H I rotation curve with the analytic function

$$V_{\text{PE}}(R) = V_0 \left(1 - e^{-R/R_{\text{PE}}}\right) \left(1 + \frac{\alpha R}{R_{\text{PE}}}\right). \quad (3)$$

This is the Polyex model from [Giovanelli & Haynes \(2002\)](#). V_0 , R_{PE} , and α , respectively, determine the amplitude of the outer rotation curve, the exponential scale length of the inner rotation curve, and the slope of the outer rotation curve.

3.2 H I mass surface density profiles

In this work, the total baryon mass surface density profiles are calculated as

$$\Sigma_b(R) = \Sigma_{\text{HI+He}}(R) + \Sigma_*(R), \quad (4)$$

where $\Sigma_{\text{HI+He}}(R)$ is the measured H I mass surface density profile scaled by a factor of 1.342 to account for the presence of Helium ([Izotov et al. 2014](#)) and $\Sigma_*(R)$ is the measured stellar mass surface density radial profile. $\Sigma_b(R)$ has units of $M_\odot \text{ pc}^{-2}$.

The measured H I surface density profiles of almost all the galaxies in [Swaters et al. \(2009\)](#) have an exponential behaviour in their outer parts. [Swaters et al. \(2002\)](#) give the scale length of each galaxy as determined from a fit to its outer disk. However, many of the galaxies exhibit a central depression of H I, and [Swaters et al. \(2002\)](#) make no attempt to model this. Simply extrapolating the fitted exponentials from the outer to the inner disks will result in significant over-estimates of the central H I masses. Therefore, the H I surface density profiles were re-measured using the 30 arcsec H I total intensity maps. The position angle and inclination of each galaxy was calculated by fitting an ellipse to a thin ribbon of H I flux in the outer H I disk of each galaxy. These orientation parameters were then used to calculate the azimuthally-averaged H I mass surface density in concentric ellipses of width 15 arcsec. To properly calibrate the resulting profiles, they were each scaled by a constant factor to ensure that the total H I mass within 3.2 R -band disk

scale lengths was equal to $\pi \cdot (\langle \Sigma_{\text{HI}} \rangle_{3.2h})^2$, where $\langle \Sigma_{\text{HI}} \rangle_{3.2h}$ is the average H I mass surface density within 3.2 R -band disk scale lengths given in Table A.2 of [Swaters et al. \(2002\)](#). In [Swaters et al. \(2002\)](#), the shortest baselines for the WHISP observations are stated to be 36 or 72 m. The observations are therefore less sensitive to structures more extended than 5 or 10 arcmin. All but three of the galaxies used in this work are smaller than 5 arcmin, and all of them are smaller than 10 arcmin. The total H I fluxes are therefore generally expected to be well determined.

3.3 Stellar mass surface density profiles

The R -band properties of the galaxies given in Tables 2 and 3 of [Swaters et al. \(2009\)](#) are used to generate stellar surface brightness profiles. These profiles represent only the exponential disk components of the galaxies, no attempt was made to model the central components. However, relatively few of the galaxies used in this work show a significant central excess of light. The radius lever arm in $\vec{r} \times \vec{v}$ is small near the centre of any galaxy, meaning that and stellar mass contained within a bulge will not contribute significantly to the total specific baryon angular momentum. Furthermore, most galaxies are H I-dominated in terms of their baryon mass. The effects of neglecting the central light components are therefore expected to be negligible in terms of the j_b and M_b measures derived in this work. The galaxy distances are used to convert the surface brightness profiles to units of L_\odot/pc^2 . In order to convert them to stellar mass surface density profiles (M_\odot/pc^2), an R -band mass-to-light (M/L) ratio is calculated for each galaxy using one of the prescriptions from [Bell & de Jong \(2001\)](#) relating optical M/L ratios and colours of integrated stellar populations. The relation based on their mass-dependent formation model with bursts is used:

$$\log_{10} \left(\frac{M/L}{M_\odot/L_\odot} \right) = 0.851(B - R) - 0.820. \quad (5)$$

Finally, having generated $V_{\text{PE}}(R)$ and $\Sigma_b(R)$ for each galaxy, M_b and J_b are calculated using eqns. 1 and 2.

4 RESULTS AND DISCUSSION

Figures A1 to A4 show the $V_{\text{PE}}(R)$, $\Sigma_{\text{HI+He}}(R)$, $\Sigma_b(R)$, and $j_b(< R)$ profiles for all galaxies used in this study. Table 1 lists the best-fit rotation curve parameters, R -band mass-to-light ratios, and M_b , J_b , j_b measures. Some of the best-fit rotation curve parameters are clearly unphysical. (e.g. $R_{\text{PE}} = 1030$ kpc for UGC 1281), but they are used anyway given that main objective is to fit a smooth curve that accurately represents the measured rotation velocities. The distribution of R -band M/L ratios is shown in Fig. 1. Clearly, the large majority of galaxies have $M/L < 1 M_\odot/L_\odot$. Fig. 2 shows the gas fraction of each galaxy as a function of stellar mass. Almost all galaxies with $M_* \lesssim 10^{9.3} M_\odot$ are gas dominated - many of them by a factor of 10 to 100.

The main result from this work, the relation between j_b and M_b , is shown in Fig. 3. Black circles represent the WHISP galaxies from this study, blue squares the gas-rich dwarf galaxies from [Chowdhury & Chengalur \(2017\)](#), green triangles the 16 spiral galaxies from THINGS studied by

Table 1. Best-fit rotation curve parameters, mass-to-light ratios, and M_b , J_b , j_b measures for all the galaxies in this study. Column 1 gives the UGC number of each galaxy. Columns 2 - 4 give, respectively, the amplitude (in units of km s^{-1}) of the outer rotation curve, the exponential scale of the inner rotation curve (in units of arcsec), and the slope of the outer rotation curve. Column 5 gives the R -band mass-to-light ratio. Columns 6 - 8 give, respectively, the total baryon mass (in units of $10^8 M_\odot$), the total baryon angular momentum (in units of $10^{10} M_\odot \text{ kpc km s}^{-1}$), and the specific baryon angular momentum (in units of kpc km s^{-1}).

UGC	V_0	R_{PE}	100α	M/L	M_b	J_b	j_b
2023	77.2	77.2	23.2	0.78	7.7	11.6	150.8
2034	29.1	12.3	6.2	1.04	13.8	20.6	149.6
2455	9.6	2.7	11.9	0.36	16.4	21.8	132.9
3371	99.1	66.0	-2.8	1.87	26.0	111.0	426.2
3711	92.2	12.0	0.3	0.46	7.0	14.0	198.3
3966	42.7	10.2	2.1	0.08	1.4	1.1	76.8
4173	27.9	20.3	14.0	2.88	40.1	132.0	329.0
4305	43.1	64.4	-4.9	0.14	7.0	7.1	100.9
4325	96.1	22.8	-0.7	0.29	11.0	30.7	279.1
4499	75.8	33.4	-0.2	0.35	14.2	36.3	255.4
4543	56.5	2.4	0.3	0.56	96.1	708.5	736.5
5272	9.2	9.1	58.8	0.20	1.8	1.0	57.0
5414	51.6	31.4	8.8	1.11	13.3	20.2	150.7
5721	90.3	27.1	-1.5	0.20	5.9	13.5	227.6
5829	23.6	14.9	17.2	1.55	22.1	48.3	218.6
5918	29.9	16.0	6.6	1.22	3.1	3.8	123.9
6446	68.0	18.6	2.0	1.94	42.4	125.2	295.2
6628	42.3	12.3	-0.0	1.60	48.7	99.0	203.1
7047	5.9	2.3	13.8	0.25	1.2	0.5	39.8
7232	11.7	10.0	46.0	0.95	1.7	0.4	25.3
7261	70.5	15.9	1.1	0.50	11.0	28.9	261.7
7323	988.5	920.0	-258.1	0.54	20.1	55.0	272.5
7399	89.5	20.5	1.6	0.50	7.7	18.7	241.2
7524	79.9	120.6	0.9	0.97	22.8	70.1	307.1
7559	103.6	160.3	-52.4	0.25	0.7	0.2	35.5
7608	68.4	50.0	4.4	0.35	6.3	12.4	195.8
7690	67.3	12.3	-2.0	0.90	7.2	6.2	85.4
7866	20.1	17.9	10.9	0.40	1.4	0.6	45.6
7971	571.1	535.0	-281.9	1.02	7.2	5.2	72.9
8490	78.9	29.9	-0.0	0.28	6.8	16.6	243.6
9211	91.0	42.4	-8.0	0.52	9.8	24.5	249.3
9992	30.1	6.3	1.0	0.69	3.0	2.1	69.5
10310	78.5	25.3	-1.1	0.36	16.0	53.1	330.2
11861	206.9	58.2	-7.7	0.86	208.8	3178.2	1522.1
12060	75.1	13.8	-0.1	1.93	33.8	108.9	322.3
12632	60.4	34.6	3.4	0.19	10.6	34.0	318.7
12732	59.4	20.4	5.4	1.04	40.5	273.5	673.8

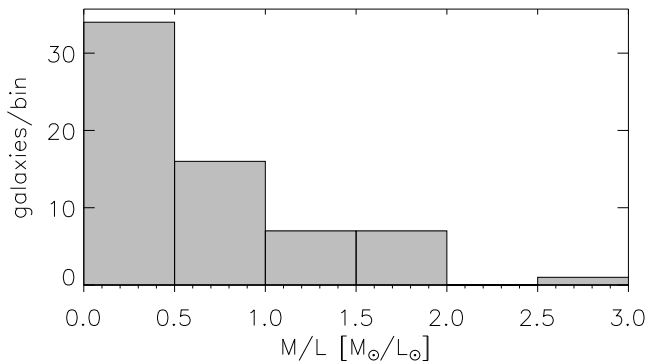


Figure 1. Distribution of R -band mass-to-light ratios for the galaxies used in this study, calculated using the prescription from Bell & de Jong (2001) given in Eqn 5.

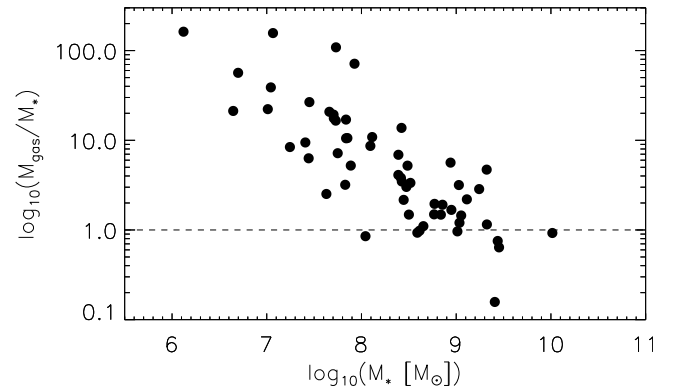


Figure 2. Gas fraction as a function of stellar mass for the galaxies used in this study. $M_{\text{gas}} = 1.342 \times M_{\text{HI}}$ is used to account for the presence of helium and other metals. Clearly, almost all galaxies with $M_* \lesssim 10^{9.3} M_\odot$ are gas dominated.

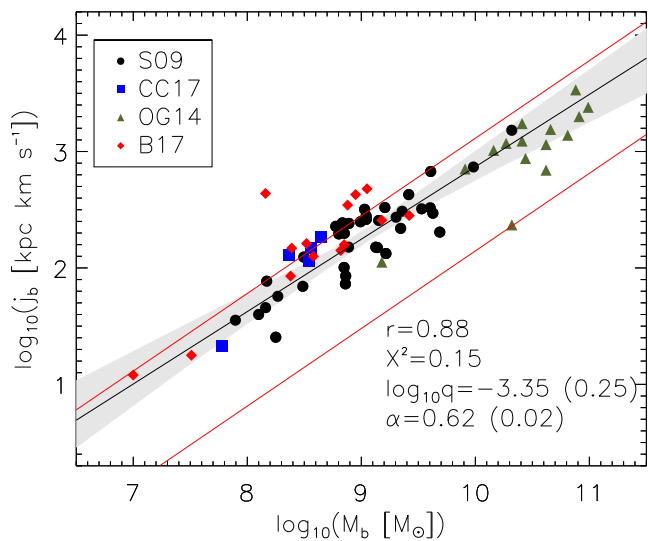


Figure 3. Specific baryon angular momentum as a function of baryon mass. The galaxies used in this study are represented by the black circles. The best-fit relation given by $j_b = qM_b^\alpha$, with $\alpha = 0.62 \pm 0.02$ and $\log_{10} q = -3.35 \pm 0.25$, is represented by the solid black line. The Pearson correlation coefficient for the data is $r = 0.88$. The grey-shaded region is based on the jackknifing method used to estimate the uncertainties in α and $\log_{10} q$, it represents the maximum range in j_b values from the best-fit relation for any given value of M_b . Also shown are the gas-rich galaxies from Chowdhury & Chengalur (2017) (blue squares), the 16 THINGS spiral galaxies from Obreschcow & Glazebrook (2014) (green triangles) and the 14 LITTLE THINGS galaxies from Butler et al. (2017) (red diamonds). The solid red lines represent the theoretically expected range of the $j_b - M_b$ relation.

Obreschcow & Glazebrook (2014), and red diamonds the 14 dwarf Irregular galaxies from the LITTLE THINGS sample (Hunter et al. 2012) studied by Butler et al. (2017). The jackknifing method was used to derive the linear relation between $\log_{10} M_b$ and $\log_{10} j_b$: a first-order polynomial was fit to each of 10^4 randomly-selected data subsets of 29 galaxies. For the relation $j_b = qM_b^\alpha$, a straight-line in $\log_{10} j_b - \log_{10} M_b$ space has slope α and y-axis intercept $\log_{10} q$. Figure 4 shows the distributions of α and $\log_{10} q$ based on the 10^4 jackknife iterations. The distributions are clearly almost Gaussian in shape. The mean parameter values are $\langle \alpha \rangle = 0.62$ and $\langle \log_{10} q \rangle = -3.35$. These mean values are represented by the solid black line in Fig. 3. The standard deviations of the α and $\log_{10} q$ distributions are $\sigma_\alpha = 0.02$ and $\sigma_{\log_{10} q} = 0.25$, respectively. The correlation between the measured values of j_b and those predicted by the best-fit line has a Pearson correlation coefficient of 0.88. The reduced χ^2 of the fit is 0.15 dex. For any value of $\log_{10} M_b$ the grey-shaded region in Fig. 3 represents the maximum range of $\log_{10} j_b$ values spanned by the 10^4 first-order polynomials fitted to the data in the jackknifing process.

Romanowsky & Fall (2012) and Obreschcow & Glazebrook (2014) both provide equations for the theoretical link between j and M . Obreschcow & Glazebrook (2014) show that for the baryonic case adopting a local $H =$

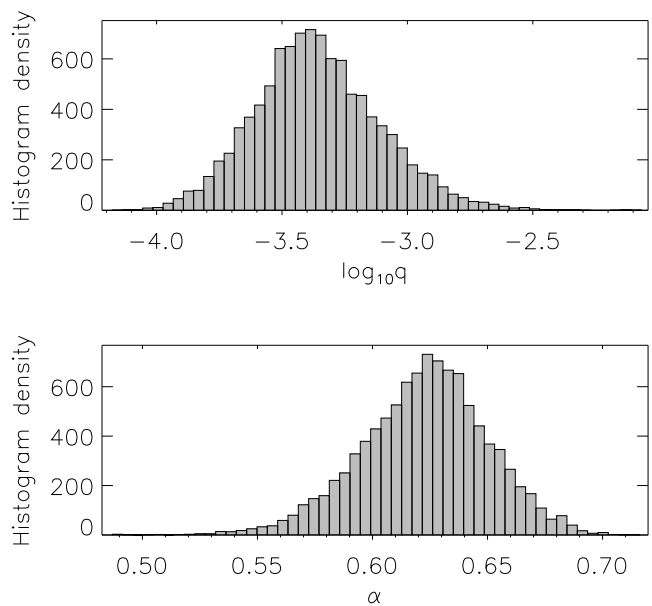


Figure 4. Distribution of best-fit α and $\log_{10} q$ from the jackknifing method used to quantify the measurement uncertainties.

$70 \text{ km s}^{-1} \text{ Mpc}^{-1}$, the relation is

$$\frac{j_b}{10^3 \text{ kpc km/s}} = 1.96 \lambda f_j f_M^{-2/3} \left(\frac{M_b}{10^{10} M_\odot} \right)^{2/3}, \quad (6)$$

where λ is the dimensionless spin parameter dealing with the halo angular momentum of a galaxy (Steinmetz & Bartelmann 1995), f_j is defined as the ratio of the specific angular momentum of the baryons to that of the CDM halo, and f_M is defined as the ratio of the baryon mass to halo mass. Using various results from the literature, Obreschcow & Glazebrook (2014) suggest the factor $1.96 \lambda f_j f_M^{-2/3}$ can vary between 0.14 and 1.3. The two red lines in Fig. 3 represent the resulting range in j_b values. Clearly, the $j_b - M_b$ relation found in this work is consistent with the theoretical expectation over the entire M_b range probed by the WHISP galaxies.

The $j_b - M_b$ relation found in this work is also consistent with many of the higher mass spiral galaxies studied by Obreschcow & Glazebrook (2014). Considering only the power-law slope α , it is in fact very similar to the value of $\alpha \approx 2/3$ that Obreschcow & Glazebrook (2014) found for their full sample of THINGS spirals. However, for a fixed bulge fraction β , their power-law index is steeper ($\alpha \approx 1$). The power-law slope from this work is also consistent with the results from the Fall & Romanowsky (2013) and Romanowsky & Fall (2012) studies that considered only the stellar component of the specific baryon angular momentum. Butler et al. (2017) found their sample of low-mass dwarf Irregular galaxies to deviate from the spiral relation measured by Obreschcow & Glazebrook (2014). They show the deviation to be consistent with CDM theory once they account for a decrease in f_M with decreasing M_b . This, they show, has the effect of bending the $j_b - M_b$ relation at the low M_b end. The (j_b, M_b) measures for the WHISP galaxies presented in this work provide no clear evidence for any such deviation.

One possible explanation for differences in the results from this work and those of [Butler et al. \(2017\)](#) may be due to the fact that here the radial profiles used to calculate j_b are extrapolated only as far as the radius R_{HI} at which the face-on H I mass surface density drops to $1 M_{\odot} \text{pc}^{-2}$. [Butler et al. \(2017\)](#) produce “hybrid” radial profiles for the H I and stellar distributions of their galaxies, as well as their rotation curves, and then extrapolate those profiles out to $15r_{\text{HI}}$ ¹. [Obreschcow & Glazebrook \(2014\)](#) explicitly state that limiting Σ_{HI} to $\geq 1 M_{\odot} \text{pc}^{-2}$ decreases J_{HI} and j_{HI} by about 20 and 10 per cent, respectively. Only one of the galaxies used in this work has its rotation curve in [Swaters et al. \(2009\)](#) measured to a radius beyond R_{HI} . Most galaxies have their rotation curves measured out to a radius significantly smaller than R_{HI} . Fitting and extrapolating the rotation curves out to R_{HI} therefore already constitutes a large extrapolation of the measured data. It is possible that extrapolating significantly further would lead to large uncertainties in the rotation curves, and hence the corresponding measures of j_b . UGC 7971 and UGC 7559 are examples of galaxies with measured rotation curves from [Swaters et al. \(2009\)](#) that can easily be flat or rising at radii beyond the last measured point, yet which have their best-fit Polydex models decreasing beyond that point.

To provide some handle on the effects of profile extrapolations on the best-fit $j_b - M_b$ relation, Fig. 5 shows the change in (j_b, M_b) measures based on the profiles that are not extrapolated beyond the last measured rotation curve point from [Swaters et al. \(2009\)](#) (grey circles) and profiles that are extrapolated out to R_{HI} (black circles, as used in this work). Some (j_b, M_b) pairs do clearly shift fairly significantly within the $\log_{10} M_b - \log_{10} j_b$ plane, especially for $M_b \lesssim 10^{9.25} M_{\odot}$. However, most shifts are roughly parallel to the best-fit relation, which therefore hardly changes. Using the un-extrapolated profiles, the best-fit relation yields $\langle \alpha \rangle = 0.65 \pm 0.03$ and $\langle \log_{10} q \rangle = -3.68 \pm 0.28$, with a Pearson correlation coefficient of 0.87 and a reduced χ^2 of 0.17 dex. This relation has larger parameter uncertainties and more scatter. This could be due to the fact that the $j_b(R)$ measures have not sufficiently converged at the last-measured points on the original (un-extrapolated) rotation curves from [Swaters et al. \(2009\)](#). It would certainly be much more preferable to directly measure the various constituent profiles required to calculate j_b and M_b out to radii that ensure both quantities converge to constant values. Future projects such as the MHONGOOSE survey (<http://mhongoose.astron.nl/>) to be carried out on the new MeerKAT telescope might provide sufficiently sensitive H I observations of nearby galaxies to carry out a highly reliable study of their $j_b - M_b$ properties.

5 LOW-RESOLUTION SYSTEMATICS

The main difference between the WHISP data used in this work and THINGS data used by other investigators is the spatial resolution. The JVLA H I data cubes used by [Obreschcow & Glazebrook \(2014\)](#) and [Butler et al. \(2017\)](#)

¹ r_{HI} is the scale length of the exponential fit to the outer part (beyond the central depression) of their measured H I radial profiles.

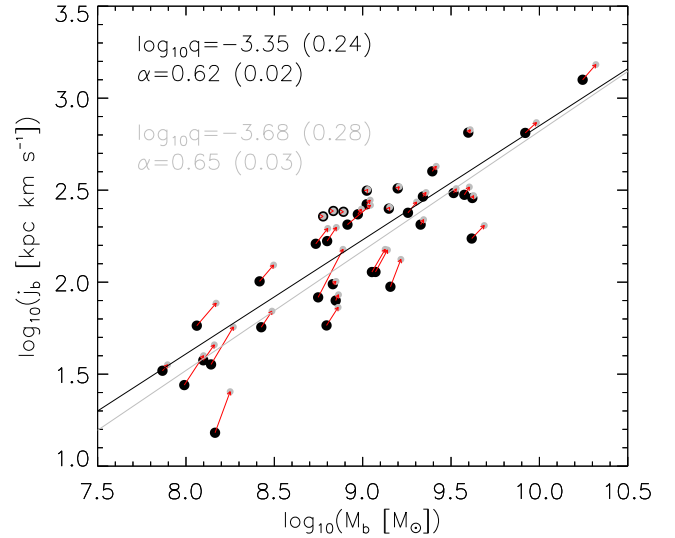


Figure 5. Comparison of measured (j_b, M_b) pairs for each galaxy used in this study based on $\Sigma_{\text{HI}}(R)$, $\Sigma_*(R)$ and $V_{\text{PE}}(R)$ profiles that are not extrapolated beyond the last measured point on the rotation curve from [Swaters et al. \(2009\)](#) (grey circles) and profiles that are extrapolated to a radius R_{HI} (black circles). Each pair of corresponding points is joined by an arrow. The black and grey lines represent the best-fit $j_b - M_b$ relations for the extrapolated and un-extrapolated profiles, respectively.

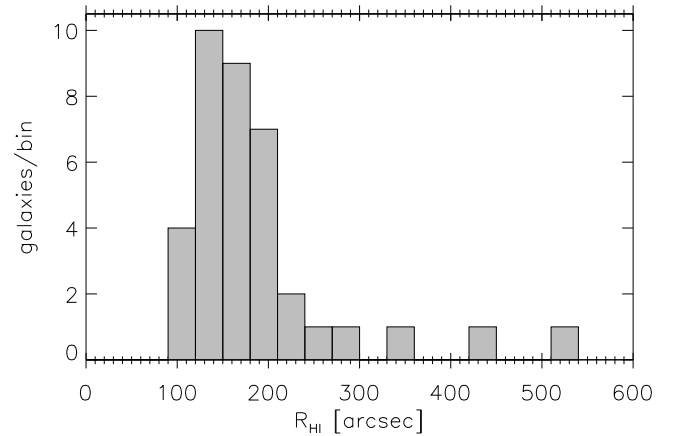


Figure 6. Distribution of HI radii for the galaxies used in this study. Given the 30 arcsec spatial resolution of the H I imaging, the majority of galaxies have 4 - 7 H I beams across their *semi*-major axis.

have spatial resolutions of $\sim 6''$, resulting in the galaxies being resolved by many beams ($\gtrsim 200$) across their major axes. In contrast, the WHISP H I total intensity maps used in this work have a resolution of 30 arcsec. Figure. 6 shows the distribution of their H I radii R_{HI} . The large majority of galaxies have 4 - 7 H I beams across their *semi*-major axis. This is as much as an order of magnitude (or more) fewer than the typical number of beams across the THINGS galaxies. A particular concern, therefore, is the possibility of the j_b and M_b measures presented in this study being systematically affected by the low spatial resolution.

In this section, two THINGS galaxies from the

Obreschkow & Glazebrook (2014) study are used to quantify the combined systematic effects of low spatial resolution on the j_b and M_b measures. NGC 925 is chosen as a low-mass system with $M_{\text{HI}} = 45.5 \times 10^8 M_\odot$ (Walter et al. 2008) and $M_* = 1.02 \times 10^{10} M_\odot$ (de Blok et al. 2008) that also has a low maximum rotation speed of $\sim 119 \text{ km s}^{-1}$ at $R \sim 13 \text{ kpc}$ (de Blok et al. 2008) that is similar to the typical galaxy used in this work. NGC 6964 is chosen as a higher-mass system with $M_{\text{HI}} = 41.5 \times 10^8 M_\odot$ (Walter et al. 2008) and $M_* = 5.88 \times 10^{10} M_\odot$ (de Blok et al. 2008) with a higher maximum rotation speed of $\sim 200 \text{ km s}^{-1}$ for $5 \text{ kpc} \lesssim R \lesssim 17 \text{ kpc}$ (de Blok et al. 2008). The naturally-weighted H I data cube of each galaxy was downloaded from the THINGS public data repository (<http://www.mpia.de/THINGS/Data.html>). Each cube was spatially smoothed on a channel-by-channel basis to a resolution corresponding to ~ 5 beams spanning the semi-major axis of the galaxy. The H I mass-size relation from Obreschkow et al. (2009) was used together with the total H I masses of the galaxies from Walter et al. (2008) to calculate $R_{\text{HI}} = 437 \text{ arcsec}$ and 646 arcsec for NGC 925 and 6946, respectively. NGC 925 was therefore smoothed to 87 arcsec spatial resolution and NGC 6946 to 129 arcsec . The smoothed cubes were spatially re-gridded to have pixel sizes equal to a third of the spatial resolution. For each smoothed, re-gridded cube, a third-order Gauss-Hermite polynomial was fit to all of its line profiles. All fitted profiles with peak amplitude greater than three times the RMS of the emission in a line-free channel were used to generate an H I total intensity map by spectrally integrating the profiles, and an H I velocity field by selecting from each profile the line-of-sight velocity corresponding to the peak amplitude. Figure 7 shows the H I maps for NGC 925 and NGC 6946. These H I maps are used to calculate values of j_b and M_b for the two galaxies that can be compared to the corresponding values from Obreschkow & Glazebrook (2014) based on the full-resolution THINGS imaging.

An H I mass surface density profile was generated for each galaxy using exactly the same method described in Sec. 3.2 for the WHISP galaxies. The $\Sigma_{\text{HI}}(R)$ profiles are shown as the red-filled circles joined by dot-dash lines in Fig. 8. The exponential stellar disks of the galaxies were modelled by fitting exponential functions to the outer parts (excluding the central bulge) of their measured stellar mass surface density profiles, kindly provided by the THINGS collaboration. The $\Sigma_*(R)$ profiles are shown as the green-dotted curves in Fig. 8. The baryon mass surface density profiles $\Sigma_b(R)$ calculated according to Eqn 4 are shown as the blue-dashed curves in Fig. 8.

The ROTCUR routine in GIPSY (van der Hulst et al. 1992) was used to fit a tilted ring model to each of the velocity fields shown in Fig. 7 in order to generate rotation curves. The same, simple approach was used for each galaxy: First, an unconstrained model in which only the expansion velocity was fixed (to 0 km s^{-1}) was used to generate a feel for the natural radial variations of the various parameters. The mean values of the dynamical centre, systemic velocity, position angle and inclination were determined and used as fixed values in the second ROTCUR iteration which then yielded the final rotation curve. The fixed values of inclination and position angle used for NGC 925 were 65.9° and 288.5° , respectively. These values are very close to the distribution of inclination and position angle that were ultimately

Table 2. j_b and M_b measures for NGC 925 and NGC 6946. Column 2 gives the measures based on the smoothed THINGS H I maps discussed and presented in Sec. 5. Column 3 gives the corresponding values from Obreschkow & Glazebrook (2014) based on the full-resolution THINGS imaging. Column 4 gives the absolute differences relative to the Obreschkow & Glazebrook (2014) measures.

	This work	OG14	% diff
NGC 925			
$\log_{10} j_b$	2.92	3.01	2.9
$\log_{10} M_b$	10.23	10.16	0.7
NGC 6946			
$\log_{10} j_b$	3.03	3.06	1.0
$\log_{10} M_b$	10.86	10.62	2.3

adopted by de Blok et al. (2008) to derive their final rotation curve (see their Fig. 67). The fixed inclination for NGC 6946 was 35.0° and the position angle 242.6° - again very similar to the distributions used by de Blok et al. (2008) (see their Fig. 83). Figure 8 shows as black-filled circles the final NGC 925 and NGC 6946 rotation curves from the tilted ring models. The best-fitting Polyex model for each is shown as the solid black curve. For comparison, the THINGS rotation curves from de Blok et al. (2008) are shown as the black dotted curves. The effects of the low spatial resolution of the data are arguably quite clearly evident. The derived rotation velocities for NGC 925 are larger than the THINGS rotation velocities by $\sim 10 \text{ km s}^{-1}$ at nearly all radii. For NGC 6946, the derived rotation velocities are lower than the THINGS rotation curve over most of the galaxy ($R \geq 225 \text{ arcsec}$).

The extrapolated Polyex model rotation curves and baryon mass surface density profiles based on the low-resolution THINGS imaging (i.e., those shown in Fig. 8) are used in equations 1 and 2 to calculate j_b and M_b measures for NGC 925 and NGC 6946. Table 2 shows the newly calculated j_b and M_b measures in the left column and the corresponding values from Obreschkow & Glazebrook (2014) in the right column. Despite having significantly lower spatial resolution, the modified THINGS maps yield very similar measures to those obtained by Obreschkow & Glazebrook (2014). When considering the logarithms of the parameters, the largest percentage difference is 2.9 per cent. Given that the Swaters et al. (2009) rotation curves are certainly of much higher quality than those derived here for NGC 926 and NGC 6946, the results from this section strongly suggest no significant systematic errors linked to the relatively low-resolution (compared to THINGS) of the WHISP imaging. The best-fit results of $\alpha = 0.62 \pm 0.02$ and $\log_{10} q = -3.35 \pm 0.25$ presented in Sec. 4 are almost certainly highly reliable and accurate.

6 SUMMARY AND CONCLUSIONS

This work uses a sample of 37 galaxies from the WHISP survey with spatially and kinematically resolved H I kinematics to study the relation between specific baryon angular momentum j_b and total baryon mass M_b over the range $10^8 \lesssim M_b/M_\odot \lesssim 10.5$. This study roughly doubles the num-

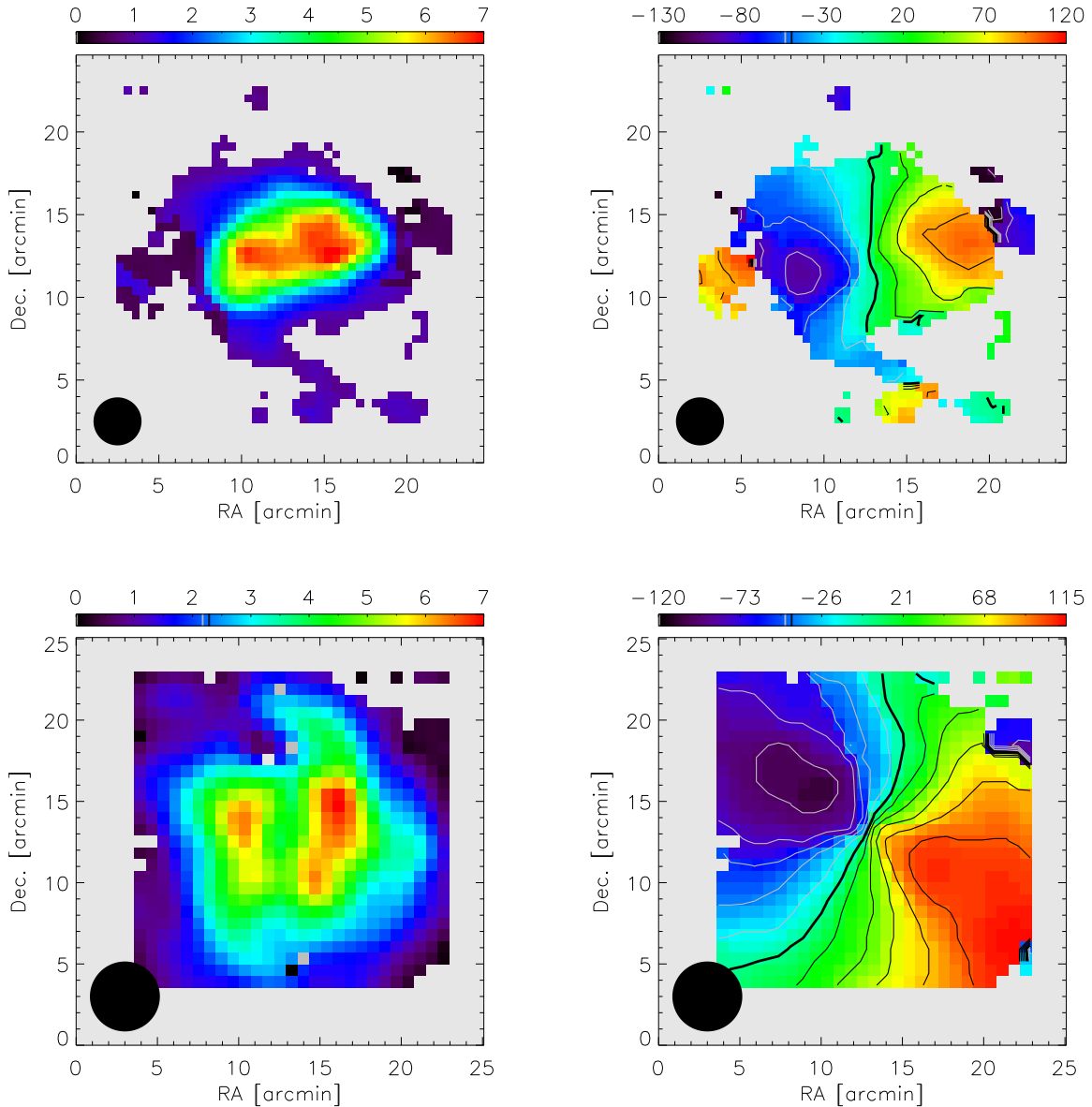


Figure 7. H I total intensity maps (left) and H I velocity fields (right) for NGC 925 (top) and NGC 6946 (bottom) based on the spatially-smoothed versions of the THINGS H I data cubes discussed in Sec. 5. These maps are used to derive the radial profiles shown in Fig. 8. The colour bar above each map gives the intensity scale in units of $M_{\odot} \text{pc}^{-2}$ and km s^{-1} for the total intensity and velocity maps, respectively. In each panel, the black-filled circle in the bottom left represents the half-power size of the Gaussian PSF. For the velocity fields, the thick black contour at the centre is at 0 km s^{-1} . The thin black/grey contours are spaced by $30/20 \text{ km s}^{-1}$ for NGC 925/6946.

ber of galaxies with $M_b \lesssim 10^{10} M_{\odot}$ used to study the $j_b - M_b$ relation.

The best-fit relation is given by $j_b = qM_b^{\alpha}$, with $\alpha = 0.62 \pm 0.02$ and $\log_{10} q = -3.35 \pm 0.25$. These best-fit parameters are shown to be robust against the effects of extrapolating the constituent radial profiles used to calculate j_b and M_b . They are also shown to be unaffected by the spatial resolution of the WHISP H I imaging. The best-fit $j_b - M_b$ relation is consistent with the theoretically expected $j_b \propto M_b^{2/3}$ relation, at least over the M_b range spanned by the WHISP galaxies. It is also consistent with the (j_b , M_b) measures of most of the higher mass spiral galaxies from [Obreschkow & Glazebrook \(2014\)](#). Unlike the results for a sample of dwarf-irregular galaxies from [Butler et al. \(2017\)](#), the results pre-

sented here do not provide an clear evidence for j_b measures that are systematically higher than the expected theoretical relation or those expected from the $j_b - M_b$ scaling of spiral galaxies.

7 ACKNOWLEDGEMENTS

The anonymous referee is thanked for providing comments and feedback that improved the overall quality of the paper. EE acknowledges the support of the South African National Astrophysics and Space Science Programme (NASSP).

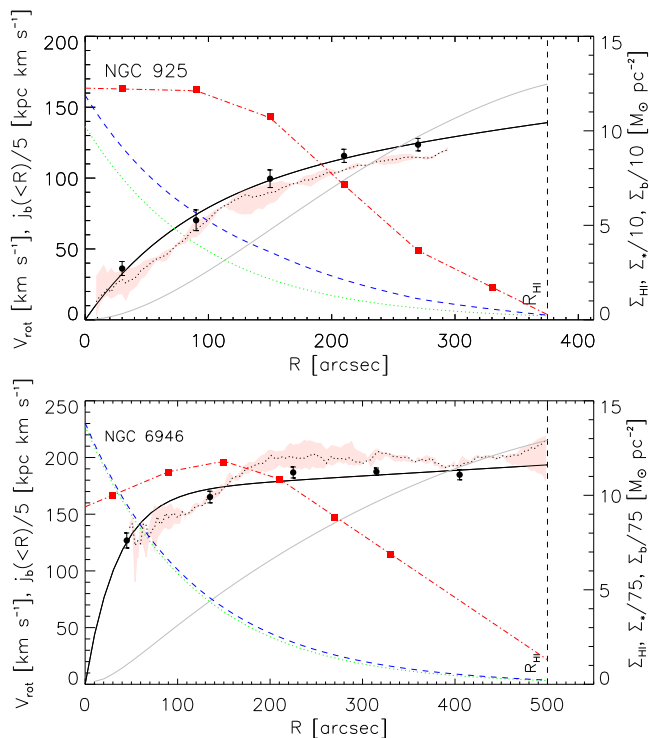


Figure 8. Various radial profiles for NGC 925 (top) and NGC 6946 (bottom) derived from the H I maps shown in Fig. 7. Black-filled circles represent the rotation curves from the tilted ring models fit to the velocity fields. The solid black curve is the corresponding best-fit Polydex model (Eqn. 3). For comparison, the rotation curves derived by de Blok et al. (2008) using the full-resolution THINGS maps are shown as black dotted curves. The salmon-shaded regions represent the difference in rotational velocities for the approaching and receding halves of the galaxies. The red-filled squares joined by the red dot-dash lines represent the H I surface densities $\Sigma_{\text{HI}}(R)$ derived from the smoothed H I total intensity maps. The green-dotted curves represent the exponential component of the stellar disk, the blue-dashed curves the baryon mass radial profile $\Sigma_b(R)$. The solid grey curves represent the cumulative specific baryon angular momentum $j_b(\leq R)$. The vertical black-dashed lines represent the H I radius R_{HI} based on the total H I mass of the galaxy.

REFERENCES

- Bell E. F., de Jong R. S., 2001, *ApJ*, **550**, 212
 Butler K. M., Obreschkow D., Oh S.-H., 2017, *ApJ*, **834**, L4
 Chowdhury A., Chengalur J. N., 2017, *MNRAS*, **467**, 3856
 Fall S. M., 1983, in Athanassoula E., ed., *IAU Symposium Vol. 100, Internal Kinematics and Dynamics of Galaxies*. pp 391–398
 Fall S. M., Romanowsky A. J., 2013, *ApJ*, **769**, L26
 Freeman K. C., 1970, *ApJ*, **160**, 811
 Giovanelli R., Haynes M. P., 2002, *ApJ*, **571**, L107
 Hunter D. A., et al., 2012, *AJ*, **144**, 134
 Izotov Y. I., Thuan T. X., Guseva N. G., 2014, *MNRAS*, **445**, 778
 Obreschkow D., Glazebrook K., 2014, *ApJ*, **784**, 26
 Obreschkow D., Croton D., De Lucia G., Khochfar S., Rawlings S., 2009, *ApJ*, **698**, 1467
 Peebles P. J. E., 1969, *ApJ*, **155**, 393
 Rogstad D. H., Lockhart I. A., Wright M. C. H., 1974, *ApJ*, **193**, 309
 Romanowsky A. J., Fall S. M., 2012, *ApJS*, **203**, 17

- Steinmetz M., Bartelmann M., 1995, *MNRAS*, **272**, 570
 Swaters R. A., Balcells M., 2002, *A&A*, **390**, 863
 Swaters R. A., van Albada T. S., van der Hulst J. M., Sancisi R., 2002, *A&A*, **390**, 829
 Swaters R. A., Sancisi R., van Albada T. S., van der Hulst J. M., 2009, *A&A*, **493**, 871
 Takase B., 1967, *PASJ*, **19**, 427
 Walter F., Brinks E., de Blok W. J. G., Bigiel F., Kennicutt Jr. R. C., Thornley M. D., Leroy A., 2008, *AJ*, **136**, 2563
 de Blok W. J. G., Walter F., Brinks E., Trachternach C., Oh S.-H., Kennicutt Jr. R. C., 2008, *AJ*, **136**, 2648
 de Vaucouleurs G., de Vaucouleurs A., Corwin Jr. H. G., Buta R. J., Paturel G., Fouqué P., 1991, *Third Reference Catalogue of Bright Galaxies. Volume I: Explanations and references. Volume II: Data for galaxies between 0^h and 12^h. Volume III: Data for galaxies between 12^h and 24^h.*
 van der Hulst J. M., Terlouw J. P., Begeman K. G., Zwitser W., Roelfsema P. R., 1992, in Worrall D. M., Biemesderfer C., Barnes J., eds, *Astronomical Society of the Pacific Conference Series Vol. 25, Astronomical Data Analysis Software and Systems I*. p. 131

APPENDIX A: RADIAL PROFILES

The next pages show the various radial profiles generated and used in this work. Each panel corresponds to a different galaxy. For each galaxy the details are as follows: the H I mass surface density profile $\Sigma_{\text{HI}}(R)$ measured from the 30 arcsec WHISP H I total intensity map is represented by the red dash-dot curve, the measured rotation curve from Swaters et al. (2009) is represented by the black circles, the model rotation curve is represented by the solid black curve, the surface brightness profile for the exponential disk component of the stellar disk $\Sigma_{*}(R)$ is represented as the green dotted curve, the total baryonic mass surface density profile $\Sigma_b(R)$ is represented by the blue dashed curve, the cumulative baryonic specific angular momentum profile $j_b(< R)$ is represented by the grey solid curve.

The UGC number of the galaxy is given above each panel. Inside each panel is given: 1) the physical length scale in units of kpc corresponding to the 30 arcsec resolution of the H I imaging, 2) its rotation curve quality parameter as detailed in Swaters et al. (2009), 3) its specific angular momentum in units of kpc km s^{-1} at radius R_{HI} , and 4) R_{HI} in units of kpc.

This paper has been typeset from a $\text{T}_{\text{E}}\text{X}/\text{L}^{\text{A}}\text{T}_{\text{E}}\text{X}$ file prepared by the author.

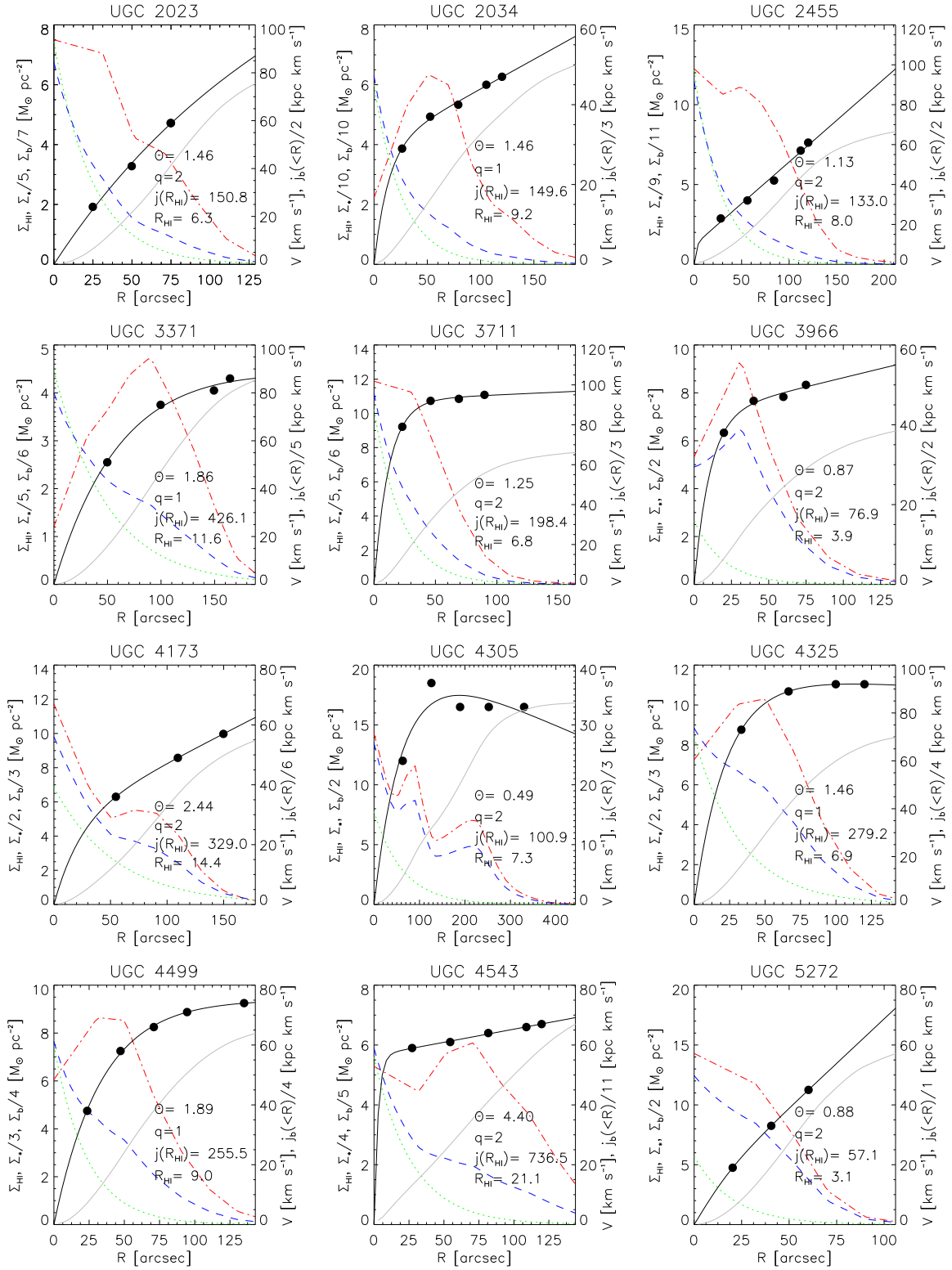


Figure A1. Various radial profiles for each galaxy used in this study. The radial profiles for Σ_{HI} , Σ_* , Σ_b , $j_b(<R>)$ and V are represented by the red, green, blue, grey and black curves, respectively. See the start of Appendix A for a detailed description the content in each panel.

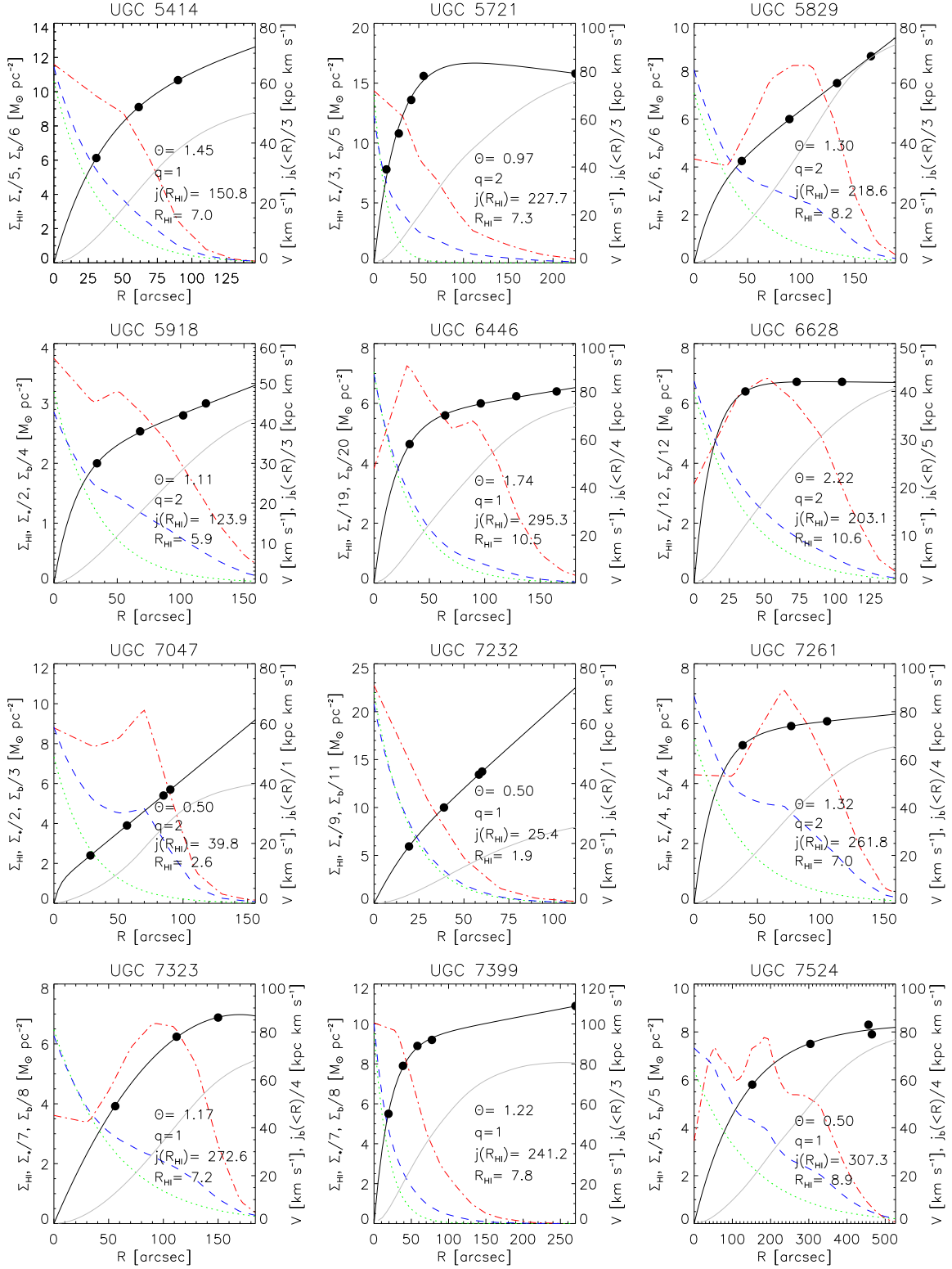


Figure A2. Various radial profiles for the galaxies used in this study. See Fig. A1 caption and the start of Appendix A for more details.

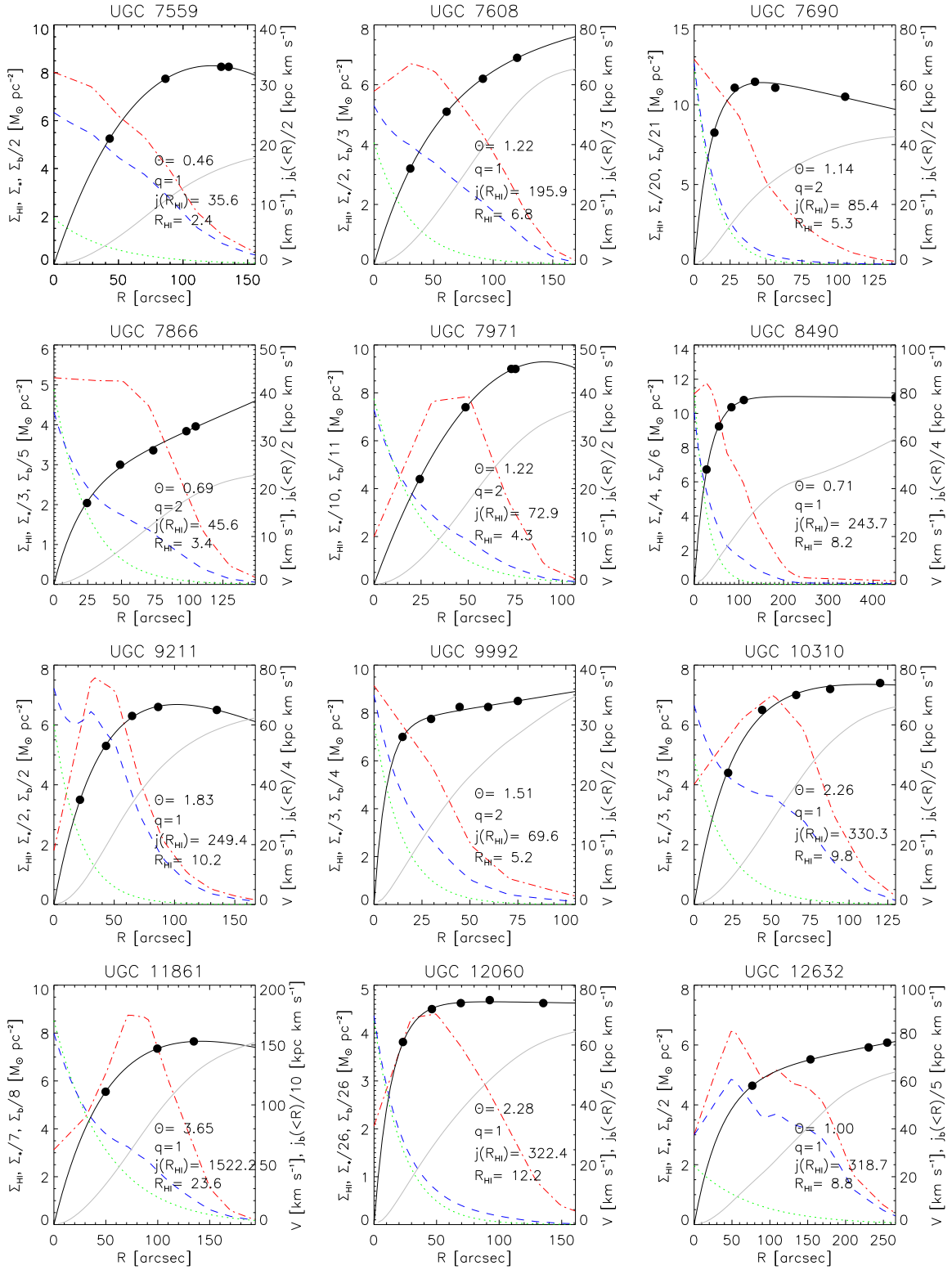


Figure A3. Various radial profiles for the galaxies used in this study. See Fig. A1 caption and the start of Appendix A for more details.

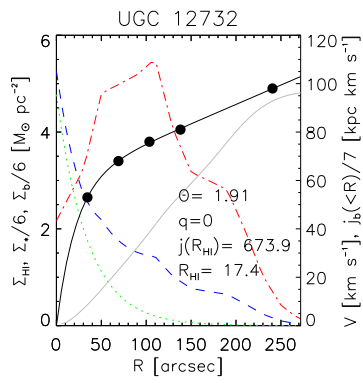


Figure A4. Various radial profiles for UGC 12732 used in this study. See Fig. A1 caption and the start of Appendix A for more details.